Creep properties of siltstone-like materials with different unloading confining pressures under seepage

Xiangdong Zhang[1], Zhongchao Zhou[1]*, Jianjun Yang[2], Shuai Pang[1], Jie Geng[1], Wenliang Li[1] and Xuefeng Zhang[1]

[1]College of Civil Engineering, Liaoning Technical University, Fuxin, Liaoning, China, [2]China Northeast Architecture Design and Research Institute Co., LTD., Shenyang, Liaoning, China

Deep enclosing rocks exhibit non-homogeneous characteristics of dense joints and fissure development. Soft rocks subjected to multiple factors, such as high stress and hydrostatic pressure, are prone to damage and significant deformation, which can lead to instability of the surrounding rocks, failure of the supporting structure, and other accidents. In this study, we investigated the creep behaviour of deep soft rocks and siltstone-like materials subjected to different unloading confining pressures coupled with a high stress field and seepage. Subsequently, the laws and behaviours of parameters, such as the transient strain, creep deformation, and creep rate were derived and analysed under various conditions. The results indicate that the radial creep curve exhibits a variation pattern similar to that of the axial creep. However, the extent of radial creep exceeds that of axial creep in soft siltstone-like rocks under unloading confining pressure conditions. We derived expressions for the constitutive relation of siltstone-like specimens under various unloading confining pressure conditions in the presence of seepage using an improved viscoelasticmodel that considered the coupling effect of fissure and seepage flow. The correlation coefficients of the calculated model values with the experimental values, as obtained by the non-linear least-squares fitting, were all above 0.9178, indicating that the proposed model can accurately characterise the creep process in fissured siltstone.

KEYWORDS

seepage, siltstone-like materials, creep, constitutive model, integrity indices

Introduction

Rock masses encountered in deep underground projects are in a complex hydrogeological and tectonic stress environment. The stress distribution in the rock mass is influenced by the complex hydrological conditions within the rock mass and the gradual development of pore-water fissures. This complex rock interaction originates from subsurface pressure. However, the original equilibrium conditions of the rock mass are affected by the stress field. Challenges related to fault fracture zones and

stress-redistribution-induced rock deterioration, which can cause major engineering disasters, are common in geotechnical engineering. Therefore, the investigation of the mechanical deformation characteristics of rock masses and creep under seepage conditions is critical for geological construction.

The rheological properties of rocks have received considerable attention since the 20th century. Du et al. (2021) studied an early monitoring and early warning system for brittle failure disasters and proposed specific coping strategies and measures for the five technical bottlenecks in the early monitoring and early warning of collapse disasters. Chen et al. (2004) proposed a fracture interaction mechanism, an equivalent extension model, and a rock creep damage-elastoplastic coupling constitutive model based on the damage fissure-related mechanics theory by using the plastic damage-fracture components in conjunction with the Kelvin model. Sha et al. (2018) established a link between the macroscopic and microscopic mechanisms of sandstone fractures based on their macroscopic and microscopic characteristics. Scanning electron microscopy (SEM) investigation revealed the seepage-creep pattern and damage mechanism in coal-bearing sandstones. Long et al. (Wang and Jiang, 2018) conducted two sets of triaxial unloading creep tests on basalt under hydrodynamically coupled conditions. They observed the tensile-shear damage pattern of basalt under unloading confining pressure and hydrodynamic coupling and reported that the relationship between the confining pressure and steady-state creep rate could be described by an exponential function. Zhang et al. (2022). Studied the fracture characteristics and strength criterion of layered sandstone through triaxial compression tests of rock samples with different bedding angles under different confining pressures. It was found that the failure mode and strength of the bedding sandstone were related to the bedding dip angle, showing obvious anisotropy. Liu et al. (2022a), Liu et al. (2022b) analysed the fracture mode of single-crack limestone under different confining pressures and water pressures based on the evolution of water inflow in ultra-deep mines and a hydrogeological model considering the interaction of multiple wells using prefabricated limestone single-crack samples. They deduced the rock compression-shear fracture criterion under the action of hydraulic coupling. Wang et al. (2017) examined the effect of internal rock crack damage on the evolution of macroscopic deformation characteristics and permeability by conducting triaxial creep-seepage-acoustic emission experiments on granite from the geological disposal area of high-level radioactive waste in Beishan, Gansu Province, at different confining pressures. Liu et al. (2021) developed a three-dimensional nonlinear creep model of deformed fissured sandstone based on the study of green sandstone under the combined action of axial and hydraulic pressures. Wang et al. (2019) studied the fracture characteristics of mudstone from the No. 12 Pingdingshan coal

mine and found that perturbation converts ductile-brittle coupled fracture to brittle fracture-dominated cleavage damage. Li et al. (2021), Du et al. (2017) conducted freeze–thaw tests on rocks to study the relationship between the natural vibration frequency and cohesion. It was found that frost heave of pore water caused crack initiation and development, forming intergranular and transgranular cracks. Uneven shrinkage and expansion of minerals are the main reasons for the internal degradation of dry rocks. Shan et al. (2019) studied triaxial creep and deformation damage in frozen laminated red sandstone around the shaft of the freezing project of the Shilawusu mine in the northwest region of China using a dynamically disturbed low-temperature rock triaxial test system and described its long-term mechanical properties and non-linear creep characteristics. Zhou et al. (2020) developed a coupled seepage evolution model and damage creep model for soft rocks and observed the deformation behaviour of soft rocks in three different creep stages. Zhao et al. (2021a), Zhao et al. (2021b) proposed a natural rock joint strength model and dual-media seepage model. The former more comprehensively reflects the relationship between the parameters affecting the joint surface topography and shear strength. The dual-media model includes equivalent continuous and discrete fractured media to study seepage-damage coupling effects in fractured rock masses, considering the massive water storage of the fracture network and the high conductivity of major large fractures.

However, these studies did not adequately consider the damage law of deep soft rocks and failed to elucidate the creep characteristics of the unloading confining pressure process in fissured soft rocks under the coupling effect of high stress and seepage fields. Therefore, we investigated the deformation and damage laws in fissured soft rocks and the creep properties of the unloading confining pressure process under the influence of seepage of fissured soft rocks. The findings of this study can guide the design of disaster warning systems to ensure construction safety and improve construction efficiency in water-rich ultra-deep mines with fissured enclosing rocks.

Test regime for unloading confining pressure creep in sandstone-like specimens under seepage action

For Muddy siltstone developed in the Hongqingliang coal mine was used as the research object to obtain the physical, chemical, and mechanical parameters *in situ* by indoor tests (Table 1). Subsequently, similar parameters and their ratios for siltstone-like materials were determined for the unloading confining pressure creep tests under different initial hydrostatic pressure conditions.

In the table, C_u is Poisson's ratio similarity ratio, C_l is the strain similarity ratio, C_k is the permeability coefficient similarity

TABLE 1 Relational expressions for the preparation of siltstone-like materials.

Similarity parameter	Similarity relation	Similarity parameter	Similarity relation
Geometric similarity	$C_u = C_l$	Model similarity	$C_G = C_\lambda$
Gravity similarity	$C_G = C_\gamma C_l$	Time similarity	$C_t = \sqrt{C_l}$
Stress similarity	$C_\sigma = C_\gamma C_l$	Hydrostatic coefficient similarity	$C_K = \sqrt{C_l}/C_\gamma$
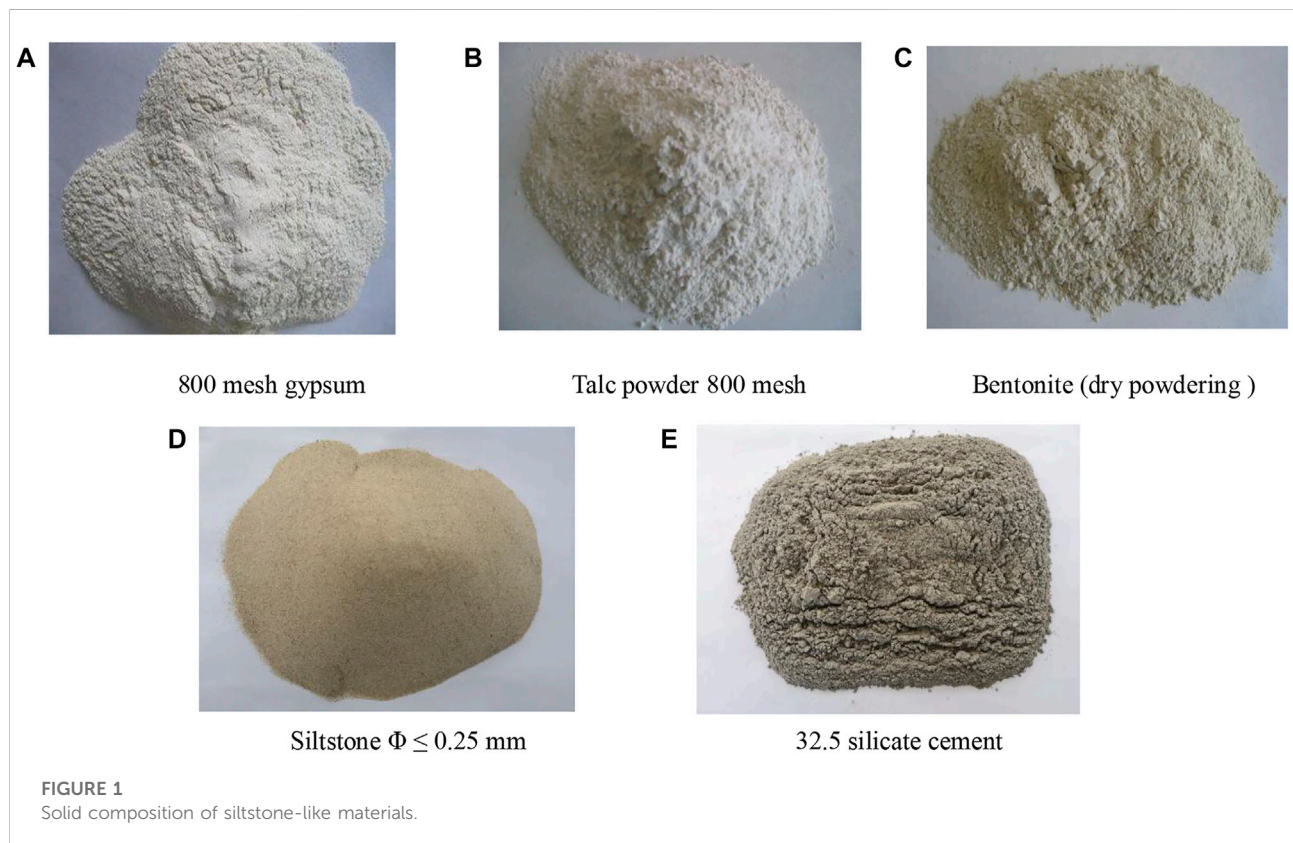
FIGURE 1
Solid composition of siltstone-like materials.

ratio, C_G is the gravity similarity ratio, C_σ is the stress similarity ratio, C_γ is the heavy similarity ratio, and C_λ is the mode force similarity ratio.

Selection of muddy siltstone-like materials

Based on long-term studies on siltstone-like materials, we determined the material specifications for this test after field sampling. Quartz sand with a grain size of less than 0.25 mm and 32.5 silicate cement was selected with saturated ammoniac thiosulfates sodium solution as the experimental water. The main factors considered were the water-binder ratio, sand-binder ratio, clay-binder ratio (the ratio of impurity components to cement mass), and mud type (talcum powder, gypsum, bentonite is dried, powdered, and passed through a 300-mesh sieve silt); the solid composition of the test materials is shown in Figures 1A-E. The specific protocol of the test was an orthogonal design with nine groups, as listed in Table 2.

Mix proportion for muddy siltstone-like specimens

Well-maintained specimens were made according to the parameters tested are shown in Table 3.

We compared the physical and mechanical parameters of muddy siltstone-like specimens in this test with those from the Hongqingliang fault fracture zone. Additionally, the permeability

TABLE 2 Preparation of fissure specimens in siltstone-like materials.

Test no.	Water-binder ratio	Sand-binder ratio	Mud-binder ratio	Type of mud
L-1	1:1.5	2.0:1	1:1.5	Talcum powder
L-2	1:1.5	2.5:1	1:1.0	Gypsum
L-3	1:1.5	3.0:1	1:0.5	Bentonite
L-4	1:2.0	2.0:1	1:1.0	Bentonite
L-5	1:2.0	2.5:1	1:0.5	Talcum powder
L-6	1:2.0	3.0:1	1:1.5	Gypsum
L-7	1:2.5	2.0:1	1:0.5	Gypsum
L-8	1:2.5	2.5:1	1:1.5	Bentonite
L-9	1:2.5	3.0:1	1:1.0	Talcum powder

TABLE 3 Physical and mechanical parameters of siltstone-like materials.

Test no.	Density ρ (g/cm³)	Compressive strength σ_c (MPa)	Tensile Strength σ_t (MPa)	Permeability coefficient K (cm/s)	Modulus of elasticity E (GPa)
L-1	2.02	28.83	2.62	$2.85 \times 10-9$	1.91
L-2	2.35	20.42	2.16	$3.50 \times 10-5$	2.40
L-3	1.90	16.28	2.85	$5.26 \times 10-8$	2.02
L-4	2.25	21.76	2.24	$8.24 \times 10-7$	2.26
L-5	2.11	22.25	2.37	$5.33 \times 10-8$	3.18
L-6	2.12	16.27	2.33	$5.09 \times 10-5$	2.18
L-7	2.28	29.90	2.47	$3.74 \times 10-5$	1.83
L-8	2.24	17.90	2.48	$1.34 \times 10-6$	2.05
L-9	2.17	16.02	2.82	$1.44 \times 10-6$	1.75

TABLE 4 Physical and mechanical parameters of siltstone-like specimens and protolith.

Materials	Density ρ (g/cm³)	Modulus of elasticity E (GPa)	Poisson's ratio μ	Compressive strength σ_c (MPa)	Tensile strength σ_t (MPa)
Muddy siltstone	2.28	4.30	0.37	22.92	2.24
Similar material (L-5)	2.11	3.18	0.35	22.25	2.37
Ratio of similitude (C)	1.08	1.35	1.06	1.03	0.95

coefficient was used as the main similarity parameter for siltstone-like specimens. The mix proportion of the L-5 scheme was most similar to the comparison results. Therefore, physical and mechanical analyses were performed on the original rock and the L-5 specimens (Table 4).

The parameter similarity ratios in Table 4 indicate that $C_E \approx C_C \approx C_{\sigma c} \approx C_{\sigma t} \approx 1$ and $C_\gamma \approx C_u \approx C_\varphi \approx C_k \approx 1$, approximately achieving the required similarity criterion for the derivation. Therefore, the L-5 scheme was adopted to simulate the siltstone in the Hongqingliang fault zone. The

material composition of the siltstone-like specimen was cement: sand: water: talc = 2: 2.5: 2: 2.

Test regime for unloading confining pressure creep in sandstone-like specimens

Rock mass integrity characterizes the degree of development at various geological interfaces (mainly fissures) and is the most

TABLE 5 Test scheme of graded unloading confining pressure creep tests under seepage.

Specimen no.	Integrity index Kv	Initial hydrostatic pressure SP(MPa)	Initial axial pressure σ1 (MPa)	Stage I confining pressure σ31 (MPa)	Stage II confining pressure σ32 (MPa)	Stage III confining pressure σ33 (MPa)	Stage IV confining pressure σ34 (MPa)	Stage V confining pressure σ35 (MPa)
RA-2	1	2	30	18	15	12	9	6
RA-4	1	4	30	18	15	12	9	6
RA-6	1	6	30	18	15	12	9	6
RB-4	0.716	4	30	18	15	12	9	6
RC-4	0.584	4	30	18	15	12	9	6

FIGURE 2
Specimens for unloading confining pressure creep test under seepage.

basic property affecting the stability of rock masses. The current evaluation index of rock mass integrity includes rock quality designation (RQD), rock mass block index (RBI), and rock mass integrity index Kv (Wu et al., 2016). In this study, a rock mass integrity evaluation index (Kv) was used to classify the enclosing rock in the engineering field, and to calculate the integrity index Kv in the fissure and intact specimens according to the standard for engineering rock test methods (GB/T50266-2013). The calculation method is as follows.

$$K_v = \left(\frac{v_{pm}}{v_{pr}} \right)^2 \quad (1)$$

where vpm is the elastic velocity of the longitudinal wave of the fracture specimen (km/s) and vpr is the elastic velocity of the longitudinal wave of the intact specimen (km/s).

To investigate the effects of seepage and specimen integrity on the creep properties of siltstone-like specimens separately, the test was divided into two stages: a creep test of intact specimens at different initial hydrostatic pressures and a creep test at different integrity levels at the same hydrostatic pressure. According to the Raymer-Hunt-Gardner model, the longitudinal wave velocity vp

FIGURE 3
Softp-rock triaxial rheometer.

of the complete sample detected by the ultrasonic tester ranges from 2.659 to 2.830 km/s, and the average value of 2.74 km/s is assumed as the longitudinal wave velocity of the complete rock

FIGURE 4
Contrcurve of creep of siltstone under the same conditions.
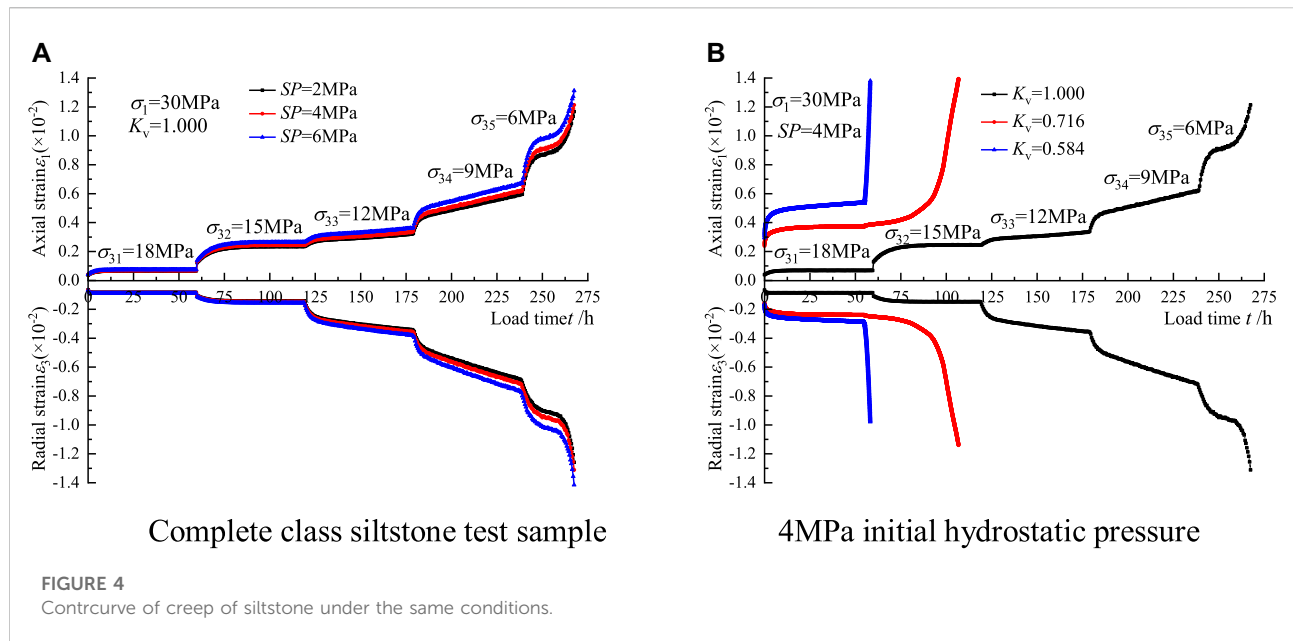
block. The integrity index of the sample whose measured value is greater than 2.74 km/s is recorded as 1, and the integrity index of the remaining samples is converted according to Eq. 1, then the wave velocities selected for the creep characteristics test under different hydrostatic pressures are 2.728, 2.738, and 2.734 Km/s. Initial permeability pressures of 2, 4, and 6 MPa were applied prior to the application of the axial pressure. For the latter, intact, relatively intact, and moderately intact siltstone-like specimens with wave velocities of 2.738, 2.317, and 2.093 km/s, respectively, were selected for testing. An additional initial permeability pressure of 4 MPa was applied before the application of the axial pressure. The test scheme is presented in Table 5, and the specimens are shown in Figure 2.

A soft rock triaxial rheometer was used for the tests (Figure 3). The axial pressure was maintained constant as the confining pressure was unloaded step-by-step. Based on the results of our long-term triaxial compression tests, the constant axial load for the unloading confining pressure creep test was set as 30 MPa. In addition, the unloading confining pressure process was divided into five stages, with an initial creep condition of 18 MPa for the enclosing rock, followed by 15 MPa, 12 MPa, 9 MPa, and 6 MPa. The test chamber was filled with oil using an external cell pressure controller. When the confining pressure was stabilised and the volume of silicone oil in the pump no longer fluctuated, the initial hydrostatic pressure was applied via an external back pressure controller in accordance with the test scheme. During this process, the hydrostatic pressure was maintained constant. When uniform droplets appeared at the outlet, the outlet was closed and the old back volume was selected. Subsequently, axial stress was gradually applied up to

30 MPa, while the axial pressure was maintained for 55 h. After the axial pressure stabilised, the confining pressure was unloaded to the specified confining pressure value at each stage until the specimen was damaged.

Creep properties of siltstone-like specimen unloading confining pressure under seepage

Deformation analysis

Creep tests were conducted sequentially according to the test scheme in Table 5. Full-process creep curves are shown in Figure 4.

The creep curve encompasses processes, such as transient deformation, decay creep, steady creep, and accelerated creep (Yang et al., 2017). Additionally, the following findings can be obtained from Figures 4A,B.

(1) When the confining pressure was 18 MPa, the creep process included only transient deformation and decay creep. When the loading duration exceeds 25 h, the rock enters a stable creep state.

(2) The creep curves included both decay creep and transient deformation creep when the confining pressure was unloaded to 15 MPa and 12 MPa. However, the creep rate was relatively low during the stable creep stage.

(3) Steady creep occurred in the intact specimens when the confining pressure was increased to 12 MPa.

Radial (axial) deformation instantaneous strain to creep ratio

Transient radial to axial creep (strain) ratio

FIGURE 5
Transient to creep ratio of radial and axial directions under percolation.
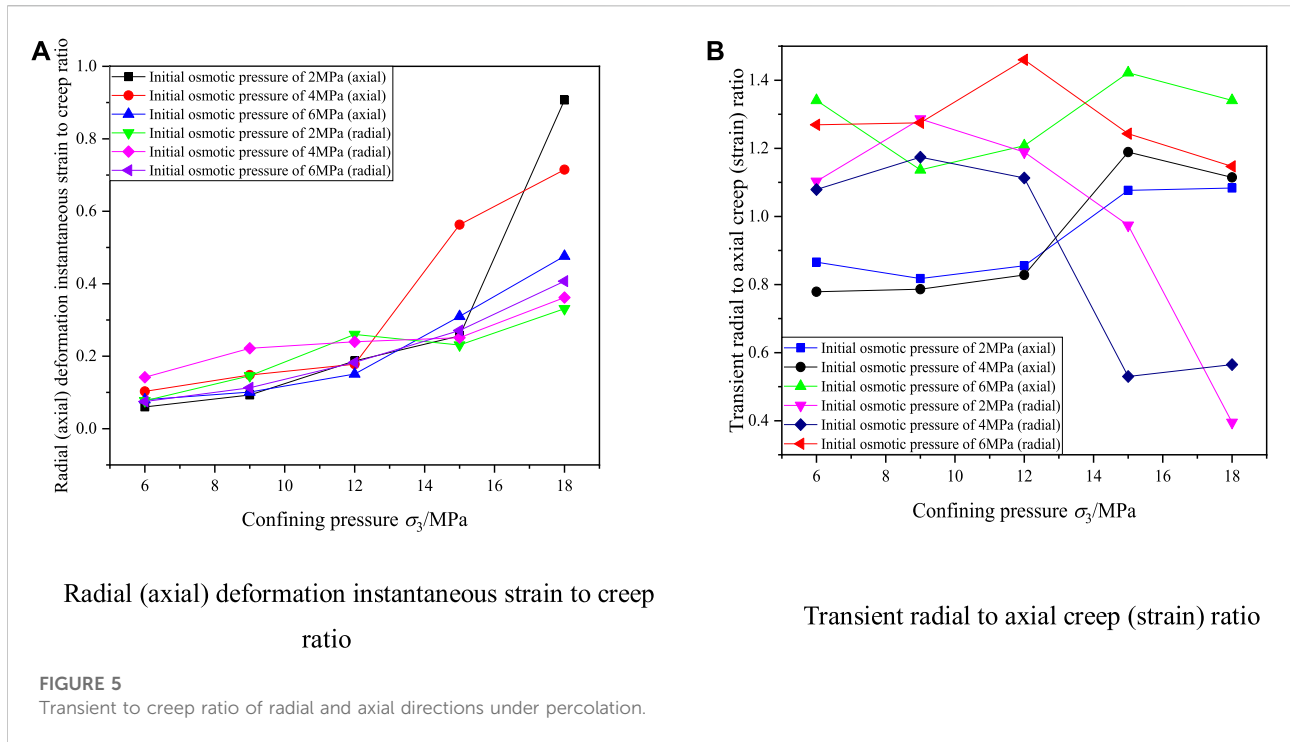
(4) When the confining pressure was unloaded to 9 MPa, the creep process included decay, steady, and accelerated unsteady creep.

(5) Under the same initial hydrostatic pressure condition, as the integrity index decreased, both the relatively intact (K_v = 0.716) and moderately intact (K_v = 0.584) specimens experienced damage when the confining pressure was 15 MPa after the first unloading of the confining pressure.

Transient and creep deformation patterns under seepage

The unloading confining pressure creep curves for siltstone-like specimens under identical conditions are shown in Figure 4B. The ratio of transient deformation to creep deformation in the radial and axial directions in this unloading confining pressure test under different seepage effects is shown in Figures 5A,B. By analyzing the unloading confining pressure creep curves of the siltstone-like specimens under the same conditions and the radial to axial deformation ratio of the unloading confining pressure test under seepage, the following findings were obtained:

(1) Radial and axial creep curves have similar variation laws. However, under unloading confining pressure conditions, radial creep is greater than axial creep, which may be attributed to the weakening of the radial restraint due to the reduction of the confining pressure. Deformation is more likely to develop in the radial direction under constant axial loading.

(2) The development of radial strain is greatly affected as the specimen integrity index decreases. Radial creep remains lower than axial creep as both the relatively intact and moderately intact specimens were damaged at high confining pressure conditions (15 MPa).

(3) The transient axial deformation value of each group of specimens in the unloading confining pressure test under seepage is less than in axial tests.

Creep rate analysis under seepage

The subsurface water content of slate is not constant due to the different forms that the rock exists in within the waterlogged environment. Groundwater can have an important influence on the long-term stability of slate slope projects. Therefore, it is crucial to study the variation law of creep deformation rate of siltstone-like materials under unloading confining pressure conditions. The first-order derivation of the creep test results was performed using Origin software. Since the rate curve of specimen RA-6 is similar to that of specimens RA-2 and RA-4 and therefore not listed, the creep process rates of specimens RA-2, RA-4, RB-4, and RC-4 curve, as shown in Figures 6A–H.

The above unloading confining pressure creep strain rate curves indicated the following:

(1) The creep rates of intact siltstone-like specimens are all produced at high strain rates upon unloading the
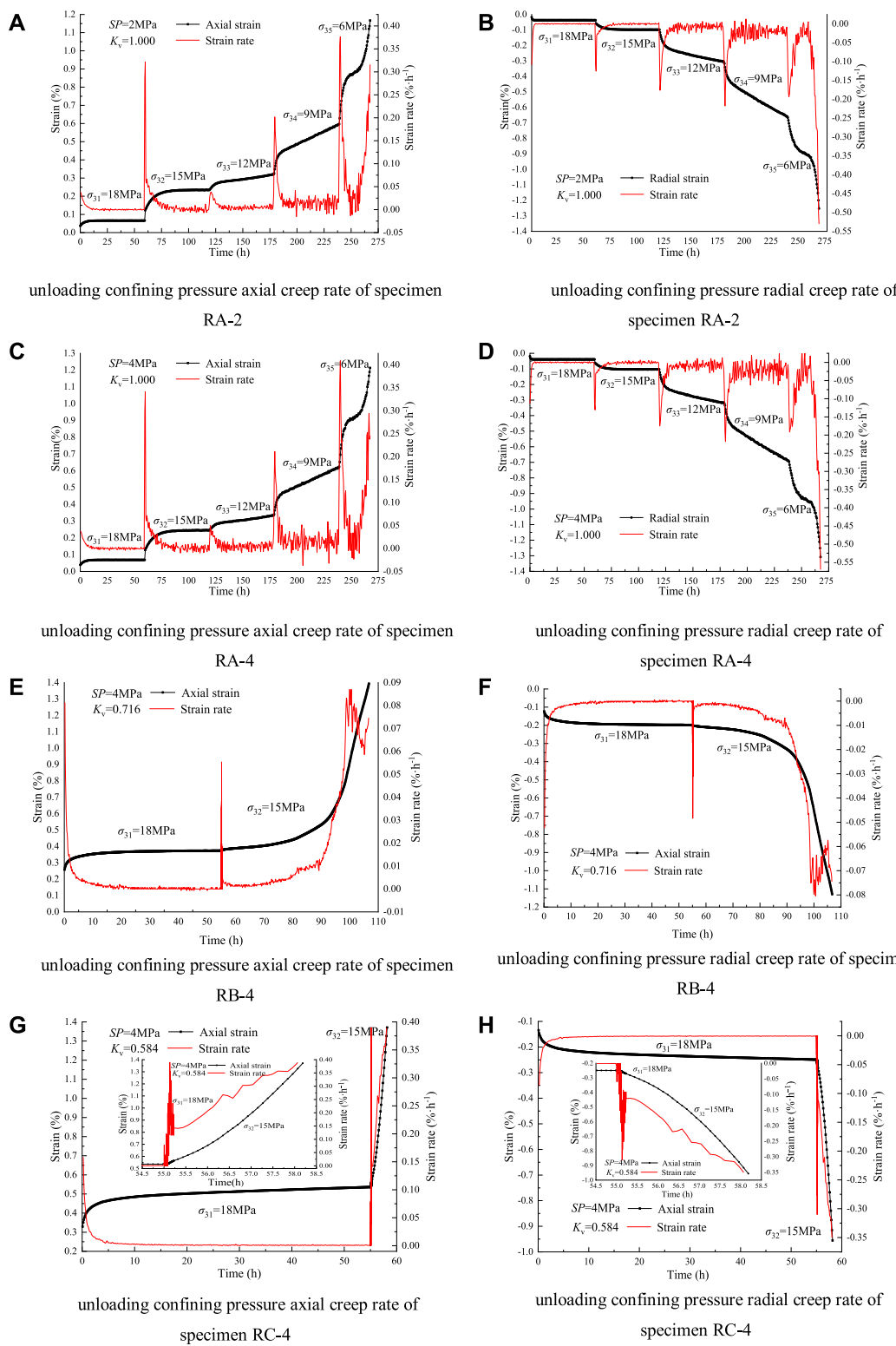
FIGURE 6
Unloading confining pressure creep rate results for specimens.

FIGURE 7
The Levenberg-Marquardt non-linear least squares method was used for the fitting analysis. The fitted curve for the theoretical creep calculation in the siltstone-like specimens at all unloading confining pressure levels was obtained for specimen RA-4, as shown in Figure 9.

FIGURE 8
HKN-based 5-component model. (1) During $\sigma < \sigma_\infty$, the NVPB in the HKN tandem model does not participate in the creep process, and its constitutive equation is as follows.

confining pressure, at which point the corresponding transient deformation corresponds to several peaks in the strain-rate curve. Subsequently, the creep rate decreased in a curvilinear pattern, indicating a decay creep stage. Then, the rate undergoes fluctuations: for stable creep, the creep deformation is constant, and the creep rate is zero.

(2) If the decay rate was >0%•h^{-1} (under normal conditions, the rate was <0.05%•h^{-1}), at which time steady creep occurred, and the strain curve increased at a certain slope. For creep rate curves that partially produce accelerated creep, the creep rate increases, resulting in accelerated creep and causing damage to the specimen.

(3) The variation trends of the radial and axial creep rates are almost identical. Additionally, the creep rate of the former was greater than that of the latter in the later stages of accelerated creep, especially at higher initial hydrostatic pressures.

Creep model under seepage

Improvements to the creep model

These results demonstrate that the coupled creep test curves of the prefabricated siltstone samples under different initial
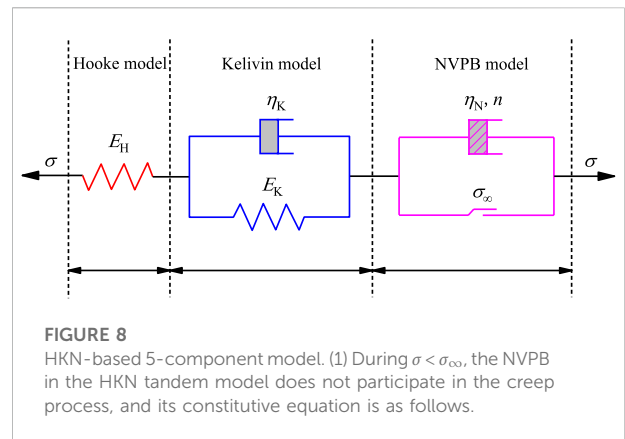
hydrostatic pressures exhibit viscoelastic plasticity. Therefore, a two-component nonlinear viscoplastic model (NVPB) identified according to the creep state index n and long-time creep strength σ_∞ was tied to the original visco-elastoplastic model (Liu et al., 2020), as shown in Figure 7A. η_N is the viscoplastic viscosity coefficient, and σ is the total stress. The creep curve of NVPB is shown in Figure 7B.

The creep constitutive relation of nonlinear visco-plastic NVPB is as follows (2):

$$\varepsilon(t) = \frac{H(\sigma - \sigma_\infty)}{\eta_N} \frac{t^n}{t_0^{n-1}} = \frac{H(\sigma - \sigma_\infty)}{\eta_N} t^n \tag{2}$$

where n is the rheological state index; t_o is the reference time, the initial value is 1; σ_∞ is the long-term strength of rock mass. Where H can be derived by the following Eq. (3).

$$H(\sigma - \sigma_\infty) = \begin{cases} 0 & \sigma < \sigma_\infty \\ \sigma - \sigma_\infty & \sigma \geq \sigma_\infty \end{cases} \tag{3}$$

When $n=1$, the creep equation of NVPB is the viscoplastic model, and the strain shows a linear relationship with time.

When $n>1$, the creep rate exhibited a positive correlation with time, which gradually increased until the specimen was destroyed.

When $n<1$, the creep rate first decreases with time and then decays to a nonzero constant iso-rate steady creep state (Zhang, 2015).

The new 5-component model, obtained by combining the Hooke, Kelvin, and NVPB models, is the HKN improvement model, as shown in Figure 8. The parameter E_H in the figure is the elastic modulus, E_K is the viscoelastic modulus, η_k is the elastic viscosity coefficient, η_N is the viscoplastic viscosity coefficient, and σ is the total stress.

$$\sigma + \frac{\eta_K}{E_H + E_K} \dot{\sigma} = \frac{E_H E_K}{E_H + E_K} \varepsilon + \frac{E_H \eta_K}{E_H + E_K} \dot{\varepsilon} \tag{4}$$

where $\dot{\sigma}$ is the stress rate and $\dot{\varepsilon}$ is the strain rate.

Substituting $\sigma = \sigma_0 H(t)$ into Eq. 4, the Laplace transformation is expanded as:

$$\tilde{\varepsilon} = \frac{\sigma_0}{E_H s} + \frac{\sigma_0}{s(\eta_K s + E_K)} \qquad (5)$$

where $\tilde{\varepsilon}$ is a Laplace transform of ε and S is a complex variable in Laplace transform. The above equation undergoes an inverse Laplace transformation to obtain the following creep equation for the constitutive relation of the model when $\sigma < \sigma_\infty$.

$$\varepsilon = \frac{\sigma}{E_H} + \frac{\sigma}{E_K}\left[1 - \exp\left(-\frac{E_K}{\eta_K}t\right)\right] \qquad (6)$$

2) When $\sigma \geq \sigma_\infty$, the HKN-based 5-component model (Zhang, 2015) is formed, and its corresponding equation of state is as follows.

$$\begin{cases} \sigma = \sigma_H = \sigma_K = \sigma_N \\ \varepsilon = \varepsilon_H + \varepsilon_K + \varepsilon_N \\ \sigma_H = E_H \varepsilon_H \\ \sigma_K = E_K \varepsilon_K + \eta_K \dot{\varepsilon}_K \\ \sigma_N = \sigma_\infty + \eta_N \dot{\varepsilon}_N / nt^{n-1} \end{cases} \qquad (7)$$

The corresponding constitutive equation is as follows.

$$p_1(\sigma - \sigma_\infty) + p_2 \dot{\sigma} + \ddot{\sigma} = \frac{E_H E_K}{\eta_K}\dot{\varepsilon} + E_H \ddot{\varepsilon} \qquad (8)$$

Solving Eq. 8 using $\sigma = \sigma_0 H(t)$, the Laplace transform is subsequently expanded as follows.

$$\tilde{\varepsilon} = \frac{\sigma_0}{E_H s} + \frac{\sigma_0}{s(\eta_K s + E_K)} + \frac{(\sigma_0 - \sigma_\infty)n!}{\eta_N s^{n+1}} \qquad (9)$$

The inverse Laplace transformation of Eq. 9 yields the following equation for the constitutive relation when $\sigma \geq \sigma_\infty$.

$$\varepsilon = \frac{\sigma}{E_H} + \frac{\sigma}{E_K}\left[1 - \exp\left(-\frac{E_K}{\eta_K}t\right)\right] + \frac{\sigma - \sigma_\infty}{\eta_N}t^n \qquad (10)$$

Combining Eqs 6,10, the following one-dimensional constitutive equation for the creep model of the fissured siltstone-like specimen is obtained.

$$\begin{cases} \varepsilon = \frac{\sigma}{E_H} + \frac{\sigma}{E_K}\left[1 - \exp\left(-\frac{E_K}{\eta_K}t\right)\right] \\ \\ \varepsilon = \frac{\sigma}{E_H} + \frac{\sigma}{E_K}\left[1 - \exp\left(-\frac{E_K}{\eta_K}t\right)\right] + \frac{\sigma - \sigma_\infty}{\eta_N}t^n \end{cases} \qquad (11)$$

$$(\sigma < \sigma_\infty)$$
$$(\sigma \geq \sigma_\infty)$$

Establishment of three-dimensional creep equations

According to elastodynamics, the stress and strain states at a point are decomposed into a spherical tensor and an adeviatoric tensor (Yang et al., 2017) as follows.

$$\left.\begin{array}{l} \sigma_{ij} = S_{ij} + \dfrac{1}{3}\sigma_{ij}\delta_{ij} \\ \\ \varepsilon_{ij} = e_{ij} + \dfrac{1}{3}\varepsilon_{ij}\delta_{ij} \end{array}\right\} \qquad (12)$$

If volumetric and deviatoric viscous strains are only associated with the spherical and deviatoric tensors, respectively, the expression for the three-dimensional tensor transformed according to Hooke's law (Jiang et al., 2021) in elastodynamics is as follows:

$$\left.\begin{array}{l} \sigma_{ii} = 3K\varepsilon_{ii} \\ S_{ij} = 2Ge_{ij} \end{array}\right\} \qquad (13)$$

where, G is the elastic shear modulus and K is the elastic volume modulus. When $\sigma < \sigma_\infty$, the elastic or viscoelastic modulus appearing in Eq. 11 is expressed in three dimensions as an elastic or viscoelastic shear modulus; by contrast, when $\sigma \geq \sigma_\infty$, the correlation expression for the resulting visco-plastic deformation, the creep-related constitutive relation in three dimensions, the corresponding yield function F, and the plastic potential function Q of the siltstone when $\sigma \geq \sigma_\infty$ are as follows:

$$\dot{\varepsilon}_{ij}^{vp} = \frac{1}{\eta_2}\left\langle \Phi\left(\frac{F}{F_0}\right)\right\rangle \frac{\partial Q}{\partial \sigma_{ij}} \qquad (14)$$

where,

$$\left\langle \Phi\left(\frac{F}{F_0}\right)\right\rangle = \begin{cases} 0 & (F < 0) \\ \\ \Phi\left(\dfrac{F}{F_0}\right) & (F \geq 0) \end{cases} \qquad (15)$$

where F_0 is the initial value of the rock yield function. Using the associated liquidity criterion, make $F = Q$, and use the power function representation of the opposite function to obtain:

$$\dot{\varepsilon}_{ij}^{vp} = \frac{1}{\eta_2}\left(\frac{F}{F_0}\right)^m \frac{\partial F}{\partial \sigma_{ij}} \qquad (16)$$

where m is the test constant, usually $m = 1$, and the three-dimensional visco-elastic-plastic creep constitutive equation can be obtained by combining Eqs 11–16.

$$\begin{cases} \varepsilon_{ij} = \dfrac{\sigma_m}{3K} + \dfrac{S_{ij}}{2G_H} + \dfrac{S_{ij}}{2G_K}\left[1 - \exp\left(-\dfrac{G_K}{\eta_K}t\right)\right] & (F < 0) \\ \\ \varepsilon_{ij} = \dfrac{\sigma_m}{3K} + \dfrac{S_{ij}}{2G_H} + \dfrac{S_{ij}}{2G_K}\left[1 - \exp\left(-\dfrac{G_K}{\eta_K}t\right)\right] + \dfrac{1}{\eta_N}\dfrac{F}{F_0}\dfrac{\partial F}{\partial \sigma_{ij}} & (F \geq 0) \end{cases}$$
$$(17)$$

In the elastic modulus G_H and viscoelastic modulus G_K, for the plastic deformation of siltstone, according to the Mohr-Coulomb yield criterion, the subsequent yield function is:
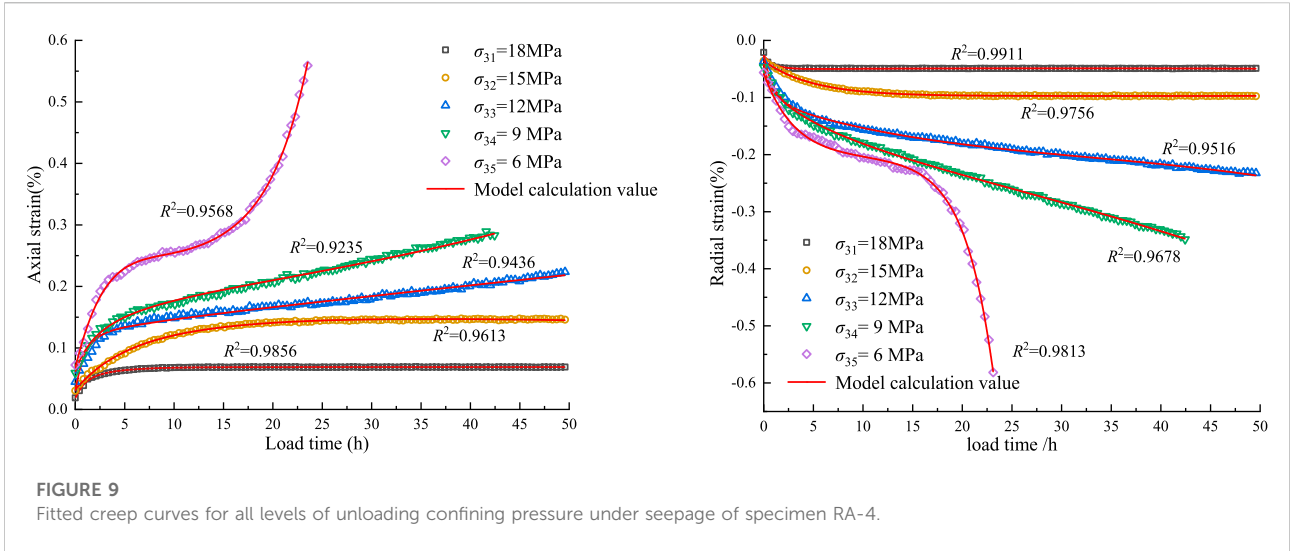
FIGURE 9
Fitted creep curves for all levels of unloading confining pressure under seepage of specimen RA-4.
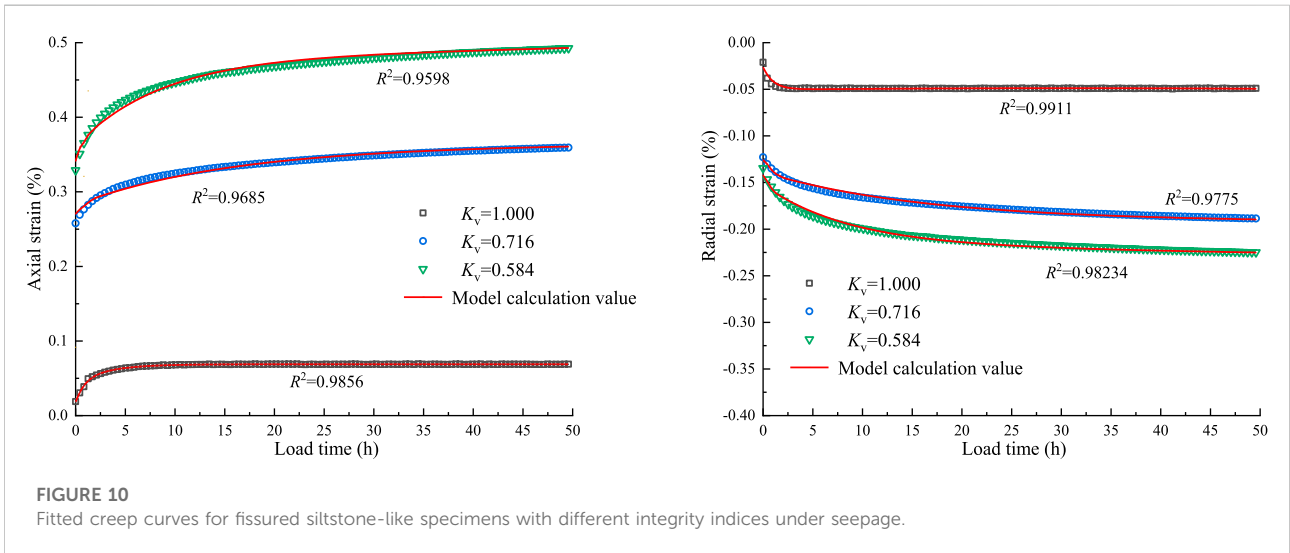
FIGURE 10
Fitted creep curves for fissured siltstone-like specimens with different integrity indices under seepage.

$$F = \sigma_1 - \sigma_3 \cdot \frac{1 + \sin\bar{\phi}(\sigma_3, \varepsilon_{ps})}{1 - \sin\bar{\phi}(\sigma_3, \varepsilon_{ps})} +$$
$$2\bar{c}(\sigma_3, \varepsilon_{ps}) \cdot \sqrt{\frac{1 + \sin\bar{\phi}(\sigma_3, \varepsilon_{ps})}{1 - \sin\bar{\phi}(\sigma_3, \varepsilon_{ps})}} \tag{18}$$

Where $\bar{c}$ represents the generalized cohesion of rock, $\bar{\phi}$ represents the generalized internal friction angle of rock, and ε_{ps} represents the equivalent plastic strain. After substituting (18) into (17), (19) can be obtained, which can be used for engineering applications.

$$\varepsilon_{ij}^{vp} = \frac{\sigma_{ij} - \sigma_\infty}{2\eta_N} t^n \tag{19}$$

Therefore, the three-dimensional visco-elastic-plastic creep Eq. 17 can be simplified as follows.

$$\begin{cases} \varepsilon_{ij} = \dfrac{\sigma_m}{3K} + \dfrac{S_{ij}}{2G_H} + \dfrac{S_{ij}}{2G_K}\left[1 - \exp\left(-\dfrac{G_K}{\eta_K} t \right) \right] & (S_{ij} < \sigma_\infty) \\[3mm] \varepsilon_{ij} = \dfrac{\sigma_m}{3K} + \dfrac{S_{ij}}{2G_H} + \dfrac{S_{ij}}{2G_K}\left[1 - \exp\left(-\dfrac{G_K}{\eta_K} t \right) \right] + \dfrac{S_{ij} - \sigma_\infty}{2\eta_N} \cdot t^n & (S_{ij} \geq \sigma_\infty) \end{cases} \tag{20}$$

In the conventional triaxial compression test, $\sigma_2 = \sigma_3$. Thus:

$$\sigma_m = \frac{\sigma_1 + \sigma_2 + \sigma_3}{3} = \frac{\sigma_1 + 2\sigma_3}{3}$$
$$S_{11} = \sigma_1 - \sigma_m = \frac{2(\sigma_1 - \sigma_3)}{3} \tag{21}$$

TABLE 6 Axial creep parameters of fractured siltstone under unloading confining pressure.

Test no.	σ_3 (MPa)	K (GPa)	α	G_H (GPa)	G_K (GPa)	η_K (GPa·h)	η_N (GPa·h)	n	R^2
RA-2	18	52.3606	0.078958	60.8093	48.3254	65.8824	—	—	0.9178
	15	16.2669	0.071877	237.0777	11.9989	37.6651	—	—	0.9948
	12	−15.6558	0.813345	50.5564	35.6184	40.6721	0.246477	0.96903	0.9312
	9	−3.395	0.838953	11.5139	11.7273	6.984	3.574547	0.873	0.9789
	6	−1.3871	0.161699	4.5396	3.9091	4.0061	3.524883	5.53773	0.9205
RA-4	18	29.4589	0.244925	115.6046	49.4603	67.415	—	—	0.9856
	15	25.317	0.557556	66.639	12.5518	39.4111	—	—	0.9613
	12	−24.3664	0.824403	67.5799	44.2029	58.8984	0.689864	0.93314	0.9436
	9	−3.4823	0.540969	9.3605	13.8419	10.9416	0.706742	0.92926	0.9235
	6	−1.5229	0.17169	5.1119	3.9576	4.0449	4.358044	5.53773	0.9568
RA-6	18	33.2904	0.015714	112.5782	51.7495	70.5384	—	—	0.9475
	15	40.7109	0.439895	50.4982	13.2502	41.5839	—	—	0.9252
	12	−36.0646	0.9603	132.9676	42.3502	50.6631	6.52131	0.93993	0.9656
	9	−15.0447	0.881439	63.6126	16.8974	10.6506	2.520545	0.74399	0.9206
	6	−2.6481	0.161699	11.6012	4.2098	4.3068	3.885141	5.5387	0.9582
RB-4	18	66.1734	0.052574	53.156	47.7143	65.0385	—	—	0.9686
	15	−0.8633	0.161699	2.4929	3.8703	3.9576	2.188223	5.53773	0.9171
RC-4	18	34.9394	0.345805	73.72	45.9004	62.565	—	—	0.9598
	15	−0.9797	0.161699	2.9585	3.6375	3.7248	3.435546	5.77353	0.9235

TABLE 7 Radial creep parameters of fractured siltstone under unloading confining pressure.

Test no.	$\sigma_3/$ MPa	α	G_H (GPa)	G_K (GPa)	η_K (GPa·h)	η_N (GPa·h)	n	R^2
RA-2	18	0.399155	138.9719	74.4766	18.2651	—	—	0.997
	15	0.194776	67.5702	12.1056	37.9949	—	—	0.9874
	12	0.893661	13.4539	15.6558	15.9371	0.690543	0.66542	0.9623
	9	0.723232	6.1789	11.349	7.5369	0.76436	0.65572	0.9651
	6	0.161699	30.9139	5.7133	9.6515	26.298058	8.29059	0.9927
RA-4	18	0.117467	123.5489	73.7879	18.0905	—	—	0.9911
	15	0.479568	136.4111	34.8909	82.0426	—	—	0.9756
	12	0.912479	48.8492	15.8498	16.1408	0.85263	0.66542	0.9516
	9	0.838662	5.141	10.6506	8.6524	2.09811	0.82353	0.9678
	6	0.161699	7.8376	5.7715	9.7291	5.325785	8.27992	0.9813
RA-6	18	0.639812	130.1546	81.4994	19.982	—	—	0.9772
	15	0.274801	148.3324	36.5981	86.0487	—	—	0.9461
	12	0.969806	15.132	16.9265	17.2369	1.408052	0.66542	0.9465
	9	0.718576	30.3125	11.2423	9.1374	1.474497	0.82353	0.9728
	6	0.161699	8.7397	6.1498	10.379	4.910431	8.28768	0.9817
RB-4	18	0.000194	144.5882	69.8885	17.1399	—	—	0.9775
	15	0.161699	6.3729	5.5193	9.2926	3.929761	8.27992	0.9577
RC-4	18	0.08051	112.4618	67.3859	16.5288	—	—	0.9823
	15	0.161699	7.5854	5.3253	8.9822	4.504971	8.28477	0.8928

Substituting Eq. 21 into Eq. 20 yields the following three-dimensional constitutive equations for conventional triaxial compression.

$$
\begin{cases}
\varepsilon = \dfrac{\sigma_1 + 2\sigma_3}{9K} + \dfrac{\sigma_1 - \sigma_3}{3G_{\mathrm{H}}} + \dfrac{\sigma_1 - \sigma_3}{3G_{\mathrm{K}}}\left[1 - \exp\left(-\dfrac{G_{\mathrm{K}}}{\eta_{\mathrm{K}}}t\right)\right] \\[3mm]
\varepsilon_{ij} = \dfrac{\sigma_1 + 2\sigma_3}{9K} + \dfrac{\sigma_1 - \sigma_3}{3G_{\mathrm{H}}} + \dfrac{\sigma_1 - \sigma_3}{3G_{\mathrm{K}}}\left[1 - \exp\left(-\dfrac{G_{\mathrm{K}}}{\eta_{\mathrm{K}}}t\right)\right] \quad (\sigma_1 - \sigma_3 < \sigma_\infty) \\[3mm]
\quad + \dfrac{2(\sigma_1 - \sigma_3) - 3\cdot\sigma_\infty}{6\eta_{\mathrm{N}}}\cdot t^n \quad (\sigma_1 - \sigma_3 \geq \sigma_\infty)
\end{cases}
$$
(22)

Establishment of the creep model under seepage

The water in the pore medium and media skeleton plays a load-bearing role. The former is referred to as the pore water pressure SP, whereas the latter exerts a skeletal bearing role as the effective stress σ_e. These two can characterize the instability deformation properties of the rock mass and are expressed as follows (Li, 2017):

$$\sigma_e = \sigma - \alpha \cdot SP$$
(23)

where α is the parameter for the seepage state.

Substituting Eq. 24 into Eq. 23 yields the seepage creep-related constitutive relation as follows:

$$
\begin{cases}
\varepsilon = \dfrac{\sigma_1 + 2(\sigma_3 - \alpha\cdot SP)}{9K} + \dfrac{\sigma_1 - \sigma_3 + \alpha\cdot SP}{3G_{\mathrm{H}}} + \dfrac{\sigma_1 - \sigma_3 + \alpha\cdot SP}{3G_{\mathrm{K}}}\left[1 - \exp\left(-\dfrac{G_{\mathrm{K}}}{\eta_{\mathrm{K}}}t\right)\right] \quad (\sigma_1 - \sigma_3 < \sigma_\infty) \\[3mm]
\varepsilon = \dfrac{\sigma_1 + 2(\sigma_3 - \alpha\cdot SP)}{9K} + \dfrac{\sigma_1 - \sigma_3 + \alpha\cdot SP}{3G_{\mathrm{H}}} + \dfrac{\sigma_1 - \sigma_3 + \alpha\cdot SP}{3G_{\mathrm{K}}}\left[1 - \exp\left(-\dfrac{G_{\mathrm{K}}}{\eta_{\mathrm{K}}}t\right)\right] \\[2mm]
\quad + \dfrac{2(\sigma_1 - \sigma_3 + \alpha\cdot SP) - 3\cdot\sigma_\infty}{6\eta_{\mathrm{N}}}\cdot t^n \qquad\qquad (\sigma_1 - \sigma_3 \geq \sigma_\infty)\ (0 < n \leq 1) \\[3mm]
\varepsilon = \dfrac{\sigma_1 + 2(\sigma_3 - \alpha\cdot SP)}{9K} + \dfrac{\sigma_1 - \sigma_3 + \alpha\cdot SP}{3G_{\mathrm{H}}} + \dfrac{\sigma_1 - \sigma_3 + \alpha\cdot SP}{3G_{\mathrm{K}}}\left[1 - \exp\left(-\dfrac{G_{\mathrm{K}}}{\eta_{\mathrm{K}}}t\right)\right] \\[2mm]
\quad + \dfrac{2(\sigma_1 - \sigma_3 + \alpha\cdot SP) - 3\cdot\sigma_\infty}{6\eta_{\mathrm{N}}}\cdot t^n \qquad\qquad (\sigma_1 - \sigma_3 \geq \sigma_\infty)\ (n > 1)
\end{cases}
$$
(24)

The nonlinear parameters α, G_H, G_K, η_K, η_N of the constitutive model are affected by time, specimen fracture development, hydrostatic pressure conditions, and the unloading stress state (Qi et al., 2012).

Creep model validation under seepage

The Levenberg–Marquardt non-linear least squares method was used for the fitting analysis. The fitted curve for the theoretical creep calculation in the siltstone-like specimens at all unloading confining pressure levels was obtained for specimen RA-4, as shown in Figure 9. The fitted curve across the theoretical results for creep calculations at different integrity index levels of the fissured siltstone-like specimens under the same seepage effect is

shown in Figure 10. The specific parameters are listed in Tables 6,7.

Based on the analysis of the creep test results in for siltstone-like specimens under seepage, the Hooke model, Kelvin model, and NVPB models were used to construct an improved visco-plastic constitutive model. This model integrated the coupling effects of fissures and seepage to derive the constitutive relation of seepage creep in siltstone-like specimens. Additionally, the model was fitted usingwith the L-M non-linear least squares method. The correlation coefficients of the calculated model relative to the experimental values all exceeded 0.9178, indicating a good fit. Overall, the model characterizes the processes of transient deformation, decay creep, steady creep, and accelerated creep in the creep process of fissured siltstone-like materials.

Conclusion

In this study, graded unloading confining pressure tests were conducted on precast siltstone-like specimens of three different integrity index types under the influence of different initial hydrostatic pressures. The NVPB was introduced to construct an improved viscoplastic constitutive model based on curve characteristics. Additionally, we obtained the constitutive relationship in seepage creep and compared the calculated values with the experimental data. The main conclusions of this study are as follows.

(1) The radial and axial creep curves exhibited a similar law of change. However, under unloading confining pressure conditions, radial creep was greater than axial creep, whereas under unloading confining pressure conditions, radial creep was greater than axial creep owing to a weakening radial constraint, as a reduction in the confining pressure weakens the weakening radial constraint. Under constant axial loading, deformation is more likely to develop in the radial direction. As the initial hydrostatic pressure increased, the radial creep of intact siltstone-like specimens also increased under pore pressure.

(2) For creep rate curves that partially produce accelerated creep, the creep rates increase and the curve rises, eventually leading to accelerated creep and damage to the specimen. The radial creep trend was similar to that of the axial creep. However, the former rate was greater than that of the latter in the later stages of accelerated creep, particularly at higher initial hydrostatic pressures.

(3) The viscoplastic constitutive model was improved using the Kelvin and NVPB models, and NVPB integrated the coupling effects of fissures and seepage. The seepage

creep-related constitutive relation was obtained for the siltstone-like specimens under unloading confining pressure conditions. The correlation coefficients between the calculated and experimental values of the model were above 0.9178, indicating that the model can well fit the creep process of siltstone.

Data availability statement

The original contributions presented in the study are included in the article/supplementary material, further inquiries can be directed to the corresponding author.

Author contributions

XZ, ZZ, JY and SP were helpful for the conception and design of this study. ZZ wrote the first draft, XZ, ZZ and WL leadership data analysis, JG and XZ interpretation results. All authors participated in the revision, reading and approval of the manuscript.

Conflict of interest

Author JY is employed by China Northeast Architecture Design and Research Institute Co., LTD.

The remaining authors declare that the research was conducted in the absence of any commercial or financial relationships that could be construed as a potential conflict of interest.

Publisher's note

All claims expressed in this article are solely those of the authors and do not necessarily represent those of their affiliated organizations, or those of the publisher, the editors and the reviewers. Any product that may be evaluated in this article, or claim that may be made by its manufacturer, is not guaranteed or endorsed by the publisher.

References

Chen, W. Z., Zhu, W. S., and Shao, J. F. (2004). Damage coupled time-dependent model of a jointed rock mass and application to large underground cavern excavation. *Int. J. Rock Mech. Min. Sci.* 41 (4), 669–677. doi:10.1016/j.ijrmms.2003.01.003

Du, Y., Xie, M., Jiang Y, J., Chen, C., J, B, N., and Huo, L, C. (2021). A review of research on the mechanism and early warning of rock collapse disasters. *Metal. Mines* (01), 106–119. doi:10.19614/j.cnki.jsks.202101008

Du, Y., Xie, M. W., Jiang, Y. J., Li, B., and Chicas, S. (2017). Experimental rock stability assessment using the frozen–thawing test. *Rock Mech. Rock Eng.* 50 (4), 1049–1053. doi:10.1007/s00603-016-1138-2

GB/T50266-2013 (2013). *Engineering rock mass test method standard*. China: National Standard of the People's Republic of China.

Jiang, T. J., Zhao, L. C., and Yu, J. X. (2021). Study on creep mechanical properties and rheological model of sandstone. *Hydropower Energy Sci.* (03), 124–128. cnki:sun:sdny.

Li, B., Zhang, G., Wang, G., and Qiao, J. (2021). Damage evolution of frozen-thawed granite based on high-resolution computed tomographic scanning. *Front. Earth Sci. (Lausanne).* 760. doi:10.3389/feart.2022.912356

Li, Q. W. (2017). *Study on rheological characteristics of seepage-stress coupling of fractured conglomerate under unloading confining pressure*. Fuxin: Liaoning Technical University, 111–122.

Liu, D. F., Liu, P. T., Zhang, Z. Y., Xi, Y. Y., and Chai, X. W. (2021). Creep character-istics of fractured sandstone under axial compression and water pressure coupling. *Eng. Sci. Technol.* 53 (01), 94–103. doi:10.15961/j.jsu

Liu, J. S., Jing, H. W., Meng, Bo, Wang, L. G., Zhang, X. D., and Yang, J. J. (2020). Study on creep characteristics and fractional creep model of weakly cemented softrock with water content. *Rock Soil Mech.* 41 (08), 412609261. doi:10.16285/j.rsm.2019.1739

Liu, J., Zhao, Y., Tan, T., Zhang, L., Zhu, S., and Xu, F. (2022). Evolution and modeling of mine water inflow and hazard characteristics in southern coalfields of China: A case of meitanba mine. *Int. J. Min. Sci. Technol.* 32, 513–524. doi:10.1016/j.ijmst.2022.04.001

Liu, Q., Zhao, Y., Tang, L., Liao, J., Wang, X., Tan, T., et al. (2022). Mechanical characteristics of single cracked limestone in compression-shear fracture under hydro-mechanical coupling. *Theor. Appl. Fract. Mech.* 119, 103371. doi:10.1016/j.tafmec.2022.103371

Qi, Y. J., Jiang, Q. H., Wang, Z. J., and Zhou, C. B. (2012). Improved three-dimensional creep constitutive equation of Nishihara model and its parameter identification. *Chin. J. Rock Mech. Eng.* (02), 347–355.

Sha, Z., Pu, H., Li, M., Cao, L., Liu, D., Ni, H., et al. (2018). Experimental study on the creep characteristics of coal measures sandstone under seepage action. *Processes* 6 (8), 110. doi:10.3390/pr6080110

Shan, R. L., Bai, Y., Sun, P. F., Sui, S. M., Huang, Y. L., and Chen, J. L. (2019). Study on triaxial creep characteristics and constitutive model of frozen layered red sandstone. *J. China Univ. Min. Technol.* 48 (01), 12–22. doi:10.13247/j.cnki.jcumt.000961

Wang, J. G., Yang, P. J., and Jin, B. (2019). Analysis of creep and meso-fracture mechanism of mudstone under dynamic and static loading. *J. China Univ. Min. Technol.* 48 (06), 1223–1229. doi:10.13247/j.cnkj.jcumt.001077

Wang, R., Zhuo, Z., Zhou, H. W., and Liu, J. F. (2017). A fractal derivative constitutive model for three stages in granite creep. *Results Phys.* 7, 2632–2638. doi:10.1016/j.rinp.2017.07.051

Wang, X., and Jiang, H. F. (2018). Research progress on unloading creep test of fractured rock mass. *Int. J. Civ. Eng. Mach. Manuf.* (1). doi:10.3389/feart.2021.79203

Wu, Q., Tang, H. M., Wang, L. Q., Le, G. P., and Fang, K. (2016). *Research on mechanical parameters and stability of fractured rock mass*. Wuhan: China University of Geosciences Press.

Yang, Y. J., Duan, H. Q., Liu, C. X., and Hao, J. R. (2017). Rational design of protective coal pillar in deep mining area considering long-term stability. *J. Min. Saf. Eng.* 34 (05), 921–927+932. doi:10.13545/j.cnki.jmse.2017.05.014

Zhang, J. H. (2015). *Study on rheological characteris-tics and control mechanism of surrounding rock of deep roadway considering seepage*. Xuzhou: doctoral dissertation of China University of Mining and Technology, 49–58.

Zhang, L., Niu, F., Liu, M., Ju, X., Wang, Z., Wang, J., et al. (2022). Fracture characteristics and anisotropic strength criterion of bedded sandstone. *Front. Earth Sci. (Lausanne).* 451. doi:10.3389/feart.2022.879332

Zhao, Y. L., Liu, Q., Zhang, C., Liao, J., Lin, H., and Wang, Y. (2021). Coupled seepage-damage effect in fractured rock masses: Model development and a case study. *Int. J. Rock Mech. Min. Sci.* 144, 104822. doi:10.1016/j.ijrmms.2021.104822

Zhao, Y. L., Zhang, C. S., Wang, Y. X., and Lin, H. (2021). Shear-related roughness classification and strength model of natural rock joint based on fuzzy comprehensive evaluation. *Int. J. Rock Mech. Min. Sci.* 137, 104550. doi:10.1016/j.ijrmms.2020.104550

Zhou, C., Yu, L., You, F., Liu, Z., Liang, Y., and Zhang, L. (2020). Coupled seepage and stress model and experiment verification for creep behavior of soft rock. *Int. J. Geomech.* 20 (9), 04020146. doi:10.1061/(asce)gm.1943-5622.0001774